PAPER

Downregulation of MIM protein inhibits the cellular endocytosis process of magnetic nanoparticles in macrophages†

Peng Zhao,[ab] Meng Cao,[ab] Lina Song,[ab] Hao Wu,[ab] Ke Hu,[ab] Bo Chen,[ab] Qiwei Wang[ab] and Ning Gu*[ab]

Magnetic nanoparticles (MNPs) are widely used in biomedical applications *in vivo*. However, the endocytosis of mononuclear phagocyte system (MPS) is still a major challenge for MNPs delivery *in vivo*. MIM (MTSS1) is a multifunctional scaffold protein to regulate both actin dynamics and membrane dynamics, which may decide the readily particles clear ability of MPS and be implicated in the cellular endocytosis. To find out the exact role of MIM plays in the nanoparticle uptake process of macrophages, we established a MIM knock-down cell line RAW 264.7^{MIM-}. The endocytosis rate and efficiency were detected to find out the differences between the normal RAW 264.7 and RAW 264.7^{MIM-} cell after 24 h of exposure to the Fe$_2$O$_3$@DMSA MNPs (70 nm hydrodynamic size). The results indicated that the clathrin-mediated endocytosis of RAW 264.7^{MIM-} cell involves fewer particles than normal RAW 264.7 cells with significant differences in the concentration ranging from 100 to 200 μg mL^{-1}. Therefore, knock-down the MIM expression in macrophage would affect the endocytosis process to iron oxide nanoparticles mainly in clathrin-mediated pathway. As a whole, our results presented here illustrated that MIM plays a positive role in the cellular endocytosis process of MNPs, which is a meaningful molecular basis for biomedical applications of nanomaterials.

1. Introduction

Magnetic nanoparticles (MNPs) are among the first nanoscale materials used in the field of biomedicine because of their unique physical, chemical, thermal and mechanical properties.[1] MNPs have a series of applications ranging from magnetic resonance imaging (MRI) contrast enhancement,[2] heating mediators for hyperthermia,[3] cell labelling and tracking,[4] cell sensing,[5] drug/gene delivery carriers[6,7] and theragnostics.[8]

Nanomaterials can enter the bloodstream following inhalation, ingestion, injection, and dermal exposure.[9] After entering the bloodstream, nanoparticles surface adsorb biomolecules, such as proteins, which act as opsonins that mark a nanomaterial for an efficient "see and process" uptake by the mononuclear phagocyte system (MPS).[10,11] In other words, once in the bloodstream, nanoparticles can readily circulate in the body while being removed by the monocytes in the blood and macrophages in organs or tissues.[9] The MPS organs become the main destination of nanoparticles circulating within the bloodstream.[12] Therefore, monocytes and macrophages are a major challenge for nanomaterial applications *in vivo*. This is why the process of nanoparticle endocytosis by macrophages is an important focus area for researchers.

Cell membranes are somewhat permeable and allow small molecules to pass through. Macromolecules must be carried into the cell in membrane-bound vesicles derived by the invagination and pinching-off of pieces of the plasma membrane in a process termed endocytosis.[13,14] Endocytosis occurs by multiple mechanisms that are generally divided into two broad categories, phagocytosis and pinocytosis. Pinocytosis occurs in all cells through at least four basic mechanisms: macropinocytosis, clathrin-dependent endocytosis, caveolin-dependent endocytosis, and clathrin- and caveolin-independent endocytosis.[15] There are many pathways for endocytosis at the cell surface that apparently proceed at the same time and are utilized by various nanoparticles to enter the cells.[16] Among all these pathways, there are two shared events. The first is to interact with the cell membrane, to decide which pathway to use for internalization of the nanoparticles. The second is that the polymerization of actin and the formation of actin cytoskeletons, which are the key components for both phagocytosis and pinocytosis.[17,18] These are decisive steps for rapid particle removal by monocytes and macrophages.

aState Key Laboratory of Bioelectronics, Jiangsu Key Laboratory for Biomaterials and Devices, School of Biological Science and Medical Engineering, Southeast University, Nanjing 210096, P. R. China. E-mail: guning@seu.edu.cn

bCollaborative Innovation Center of Suzhou Nano Science and Technology, Suzhou 215123, PR China

There is a protein superfamily called the Bin/amphiphysin/Rvs (BAR), which includes BAR/N-BAR, EFC/F-BAR and IMD/I-BAR domains. They act as central regulators involved in both membrane and cytoskeleton remodelling throughout the eukarya. Members of the superfamily are recruited from the cytoplasm. They bind the negatively charged phospholipid head groups of the membrane and cause the membrane to adopt the curvature presented by their quaternary structure (concave or convex surface), forcing the fluid-phase bilayers to bend locally. IMD domain has a convex surface, which is different from the classical concave surface, and can dimerize into a flat zeppelin shape. These are the only modules to generate membrane protrusions such as spike or filopodia or lamellipodia, which is contrary to BAR modules generating membrane invaginations or vesicle fission.[19] BAR domain proteins are also actin cytoskeleton adaptor proteins, which induce actin polymerization in the process of cytoskeleton remodelling. So, the BAR proteins could bind the cytosolic leaflet of the bilayer to trigger the formation of plasma-membrane extensions, invaginations, tubular organelles, and transport intermediates, including endocytic vesicles.[20,21]

IMD proteins are defined by the proteins MIM (missing-in-metastasis) and the IRSp53 cytoskeletal regulators. As a member of the IMD family of proteins, MIM contains several protein–protein interaction modules that suggest it functions as scaffold protein complexes at membranes and participates in endocytosis.[22]

MIM is also known as metastasis suppressor 1 (MTSS1) and is identified as a metastasis suppressor. MIM may take the driver seat during cancer metastasis.[23,24] However, there is another concept supported by accumulating evidence that MIM actually acts as a scaffold protein interacting with multiple partners to regulate both actin dynamics and membrane dynamics.[25] Functional analysis revealed that MTSS1 has several domains capable of executing corresponding functions, such as the C-terminal region WH2 domain that interacts with ATP-bound G-actin, which is involved in polymerization. IMD can bind to $PI(4,5)P_2$-enriched membranes and interact with Rac to induce membranous tubules *in vitro*.[26] MIM also has PTPδ and cortactin binding sites in the proline-rich region and three potential tyrosine phosphorylation motifs in serine-rich region.[27] MIM is a scaffold protein linking the actin cytoskeleton and the plasma membrane[28] involved in the formation of membrane protrusions, cell migration, invasion, cell–cell interaction, and endocytosis.[29]

Monocytes and macrophages are professional phagocytes. Changes in the membrane curvature and cytoskeleton deformations are required for them to participate in many physiological activities of cells. As far as we know, IMD domain proteins play important roles in a wide variety of cellular processes, such as organelle biogenesis, cell division, cell migration, secretion, and endocytosis. Microarray analyses demonstrated that MIM is the only member of the IMD domain family that was highly expressed in human blood cells, such as monocytes and macrophages.[30] Macrophages have typical pseudopodia as important parts of MPS, which can sequester foreign objects like bacteria, parasite, fungi,

nanoparticles, and drugs, *etc.* A major obstacle for drug delivery to prolong the cycle time is the high recognition and rapid phagocytosis of monocytes/macrophages on foreign objects. It is thought that the MIM protein may play a unique role in the process by which monocytes/macrophages exercised these functions.

In our research, we focused on the relationship between MIM and the MNPs enveloped *via* endocytosis by the macrophages. Iron oxide nanoparticles were used because of their good biocompatiblity.[31] The objective of this study was to explore the role that MIM played in MNP uptake by macrophages. This is important for MNP applications *in vivo*, *i.e.*, the long circulating time or retention time, accumulation in target site, *etc.* This was also a supplement to the basic research on endocytosis.

2. Materials and methods

2.1 Materials

MTSS shRNA plasmid, control shRNA plasmid-A and copGFP control plasmid were purchased from Santa Cruz Biotechnology. The shRNA Plasmid transfection reagent, transfection medium and puromycin dihydrochloride were also from Santa Cruz Biotechnology.

The antibody against MTSS1 was obtained from Santa Cruz Biotechnology, and the anti-β-actin was from Keygen Biotech.

The MTT and Annexin V-FITC/PI detection kit, RIPA lysis buffer, BCA kit and ECL detection kit were purchased from Beyotime Biotech. All other chemicals were commercially available, and the highest quality available was used.

2.2 Synthesis and characterization of Fe₂O₃@DMSA

The NPs γ-Fe_2O_3 were synthesized according to a well-established coprecipitation procedure and then coated with dimercaptosuccinic acid (DMSA) molecules.[32] The hydrodynamic diameters of Fe_2O_3@DMSA were measured by dynamic light scattering (DLS) using a Zetasizer Nano ZS (Malvern Instruments, UK). The size and surface morphology of the MNPs were observed by transmission electron microscopy (TEM, JEM-2000EX, JEOL, Japan). The sample was dropped onto a copper grid, and the grid was allowed to dry before characterization.

2.3 Cell culture

RAW 264.7 cells (Type Culture Collection of the Chinese Academy of Sciences, Shanghai, China) were maintained in DMEM (Gibco) supplemented with 10% (v/v) fetal bovine serum (HyClone, Thermo Scientific), 1% L-glutamine, and 1% penicillin/streptomycin. All the cells were incubated at 37 °C in a 5% CO_2 atmosphere. Cell culture reagents were purchased from Gibco, USA.

2.4 Transfection

For shRNA transfection, 2×10^5 cells were seeded in wells of a six well tissue culture plate, and the cultured cells were in a complete growth medium (DMEM without antibiotic) at

normal conditions until the cells gew to a 50–70% confluency. The transfection procedure was according to the manufacturer's instruction. For the selection of stably transfected cells, 48 h post-transfection, the medium was aspirated and replaced with a fresh selective medium (normal medium containing puromycin at the appropriate concentration). Approximately every 2–3 days, the medium was aspirated and replaced with freshly prepared selective media. Then, the transfected cells were harvested for subsequent analysis.

2.5 Western blot analysis

Western blotting was used to find out the effects of Fe_2O_3@-DMSA on the expression of MTSS1 (shown in ESI†) and to verify the knockdown result of MIM gene expression. Confluent cells were pelleted and then lysed with a RIPA lysis buffer. After lysis and centrifugation at $14\,000g$ for 5 minutes, the protein concentrations were determined using a BCA protein assay kit. Equal amounts of protein were separated by SDS-PAGE (10% polyacrylamide gel) and blotted onto PVDF sheets. The membranes were then probed with anti-MTSS1 antibody and horseradish-peroxidase-conjugated secondary antibody with stringent washings between each step. The anti-β-actin was used as an internal control to normalize sample loading. The targeted bands were detected by an enhanced chemiluminescence kit and visualized by an ECL system.

2.6 In vitro cytotoxicity of NPs

MTT. Cell viability was assessed using the MTT method. After 24 h exposure to MNPs at concentrations of 10 μg mL^{-1}, 50 μg mL^{-1}, 100 μg mL^{-1}, 150 μg mL^{-1}, 200 μg mL^{-1}, MTT was added to the medium at a final concentration of 0.5 mg mL^{-1} and removed after 4 h of incubation. Then, the formazan crystals were dissolved with 150 μL DMSO added into each well, and the plate was shaken for 10 minutes. The absorbance of each well was read on a microplate reader (ELx 800; BioTek, USA) at a wavelength of 490 nm. The spectrophotometer was calibrated to zero absorbance using the culture medium without cells. The relative cell viability (%) related to the control wells containing the cell culture medium without nanoparticles was calculated by $[T]/[C] \times 100$, where $[T]$ is the absorbance of the test sample and $[C]$ is the absorbance of the control sample.

annexinV/PI assay. Cells positive for apoptosis and necrosis were measured by the annexinV/PI assay. After MNPs exposure, cells were washed in binding buffer and incubated in the dark for 10 min at room temperature in 100 μL of binding buffer containing annexin V-FITC (40 μL mL^{-1}) and PI (1 μL mL^{-1}). After incubation, 400 μL of the binding buffer was added to each sample, and the cells were kept on ice. The apoptotic/necrotic cells were analyzed with FCM (FACS Calibur, BD, USA).

2.7 Transmission electron microscopy

RAW 264.7 cells were seeded in a 25 cm^2 flask at a density of 2×10^5 cells per mL and cultured overnight. Fe_2O_3@DMSA was added to a final iron concentration of 100 μg mL^{-1}. After 24 h of culture, the cells were pelleted and washed with PBS, fixed with 2.5% glutaraldehyde for 1 h, and post-fixed in 1% osmium tetroxide for 1 h. Samples were dehydrated through a series of alcohol concentrations (50%, 70%, 80%, 90%, 95%, and 100% alcohol) and were embedded in an epoxy resin. Ultrathin sections were cut at 70 nm with an ultramicrotome, transferred to the 300 mesh copper grid and stained with 5% uranyl acetate. The copper grid was observed on a transmission electron microscope (TEM, HITACHIH-600) at 80 kV.

2.8 Cellular uptake of MNPs

Cells were seeded in 6-well plates at a density of 2×10^5 cells per well and cultured overnight. Fe_2O_3@DMSA was added to reach a final iron concentration of 10 μg mL^{-1}, 50 μg mL^{-1}, 100 μg mL^{-1}, 150 μg mL^{-1}, 200 μg mL^{-1}, separately, and the cells were incubated for another 24 h at the normal culture conditions. To find out the roles of MIM in the cellular uptake of MNPs, we used two methods to detect the uptake efficiency.

o-Phenanthroline photometric method. MNPs uptake was determined using an o-phenanthroline colorimetric method.[33–35] After treatment with Fe_2O_3@DMSA, the cells were washed 3 times with PBS, then collected, pelleted and resuspended in water and vortexed to rupture the cell membranes. Aliquots of cell lysates were mixed at equal volumes (0.5 mL) with 6 mM hydrochloric acid (HCl) in order to dissolve the MNPs via incubating for 1 h at room temperature. This was followed by the addition of 0.2 mL of a 10% aqueous solution of hydroxylamine hydrochloride to reduce $Fe(III)$ to $Fe(II)$. Then, 0.4 mL of a 0.1% aqueous solution of o-phenanthroline, 0.4 mL 6 M NaOH, 1 mL ammonium acetate–acetic acid buffer were added to maintain the acidic pH for Fe–phenanthroline complex formation. The mix solution was diluted to 10 mL with deionized water and incubated for 1 h at room temperature. The absorbance was measured at 510 nm with a spectrophotometer (UV-3600, Shimadzu, Japan). The iron concentration of each sample was calculated from a standard plot and normalized to the protein concentration of the sample as determined by the micro BCA assay.[36]

SSC measurement with FCM. SSC measurement can be used to analyse the cellular uptake of NPs. Cellular granularity can change after internalizing NPs, causing significant changes in the forward light scattering. The presence of nanoparticles greatly increased the side scattering.[37] After treatment with Fe_2O_3@DMSA, the cells were then collected and washed with PBS 3 times with centrifugation at 300 g for 5 min between washes.[38] The cell pellet was resuspended in 1 mL PBS and analyzed by flow cytometry. At least 10 000 cells were analyzed for each treatment. Nanoparticle uptake was measured by flow cytometry by measuring the side scatter (SSC), a parameter that measures cellular granularity.[39]

FCM detection of MNP uptake. To determine which endocytotic pathway is involved when macrophages encounter MNPs, several inhibitors related to different endocytotic pathways were incubated separately with RAW 264.7 cells prior to MNPs treatment. These inhibitors included cytochalasin D (3 μM), nocodazole (10 μM), phenylarsine oxide (3 μM), genistein (0.1 mM). Cytochalasine D blocks actin dependent process such as macropinocytosis; nocodazole inhibits microtubule function

involved in intracellular vesicle trafficking; phenylarsine oxide inhibits the clathrin-mediated endocytotic pathway; genistein disturbs the caveolae pathways by preventing the phosphorylation of caveolin. RAW 264.7 cells were incubated with various inhibitors (Aladdin, Shanghai, China) as described with a suspension of Fe_2O_3@DMSA (100 µg mL^{-1}) for 4 h. Treated cells were then washed three times with PBS and harvested by trypsinization. After centrifugation, the cell pellet was washed once and resuspended in PBS. The effects of the inhibitors on cellular MNP uptake were examined using FCM and software Flowjo 7.6.

2.9 Immunofluorescence and co-localization assays

After 4 h of culture, the cells with the Fe_2O_3@DMSA (100 µg mL^{-1}) along with the controls were fixed in 4% formaldehyde/PBS for 15 min. When fixed, the samples were washed 3 times with PBS and incubated at 37 °C for 5 min in 1% BSA/PBS. This was followed by the addition of anti-MTSS1/FITC antibody (1 : 100 in 1% BSA/PBS, Bioss, China) and anti-clathrin/RBITC (1 : 100 in 1% BSA/PBS, Bioss, China) for 1 h (37 °C) in the dark. After a final wash, the cells were then observed under a laser scanning confocal microscope (TCS SP8, Leica, Germany).

Statistical methodology. All results are reported as the mean of three to five independent experiments, and error bars are the standard deviation (SD). Comparisons were performed using a one-tailed Student's t-test ($*P < 0.05$, $**P < 0.01$, $***P < 0.001$).

3. Results

3.1 Characterization of Fe_2O_3@DMSA

Fe_2O_3@DMSA nanoparticles were synthesised by our group. The morphology and structure of particles were observed by TEM, and the images indicated that most of the particles are quasi-spherical with an average diameter of 15 nm. The TEM image and size distribution of particles are shown in Fig. 1. Dynamic light scattering was carried out to measure the size and size distribution of Fe_2O_3@DMSA NPs, and the results are shown in Fig. 1. The average hydrodynamic size of these Fe_2O_3@DMSA NPs was about 71.6 nm in diameter. The apparent zeta potential of Fe_2O_3@DMSA was −43.9 mV.

The size of the nanoparticles played a key role in cellular uptake and biodistribution. The hydrodynamic size of the nanoparticles we used had a high endocytosis efficiency,[40] which was important for our study.

3.2 Viability/cytotoxicity studies

MTT assay is a simple, nonradioactive, colorimetric assay to measure cell cytotoxicity, proliferation, or viability. The viability of RAW 264.7 cells is decreased slightly with an increase in the concentration of the Fe_2O_3@DMSA NPs compared with the control, as shown in Fig. 2A. The data were analysed by a statistical method, and the results indicated that there is no significant statistical difference at the concentrations of 10 µg mL^{-1}, 50 µg mL^{-1}, 100 µg mL^{-1}, 150 µg mL^{-1}, and 200 µg mL^{-1}.
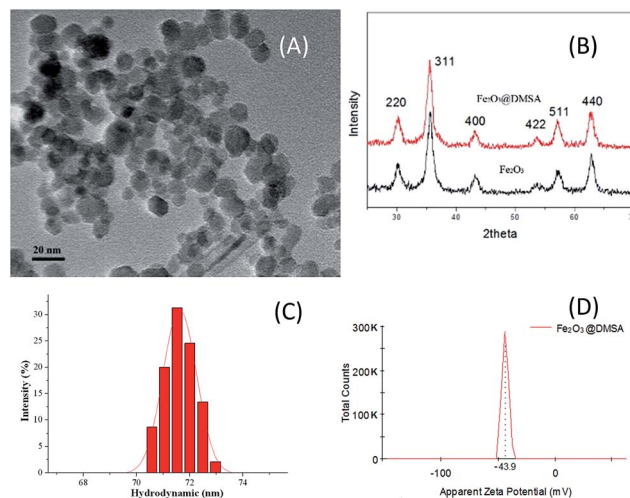
Fig. 1 Particle size analysis of Fe_2O_3@DMSA was characterized by TEM and DLS. (A) TEM showed the Fe_2O_3@DMSA diameters were 15 ± 4 nm; (B) XRD analysis of bare and DMSA coated nanoparticles; (C) DLS showed the hydrodynamic size was 71.6 nm. (D) Apparent zeta potential of Fe_2O_3@DMSA was −43.9 mV.

The results of the annexin V/PI assay in Fig. 2B showed no significant reduction in the percentage of viable cells after 24 h exposure to MNPs in the concentrations range of 10–200 µg
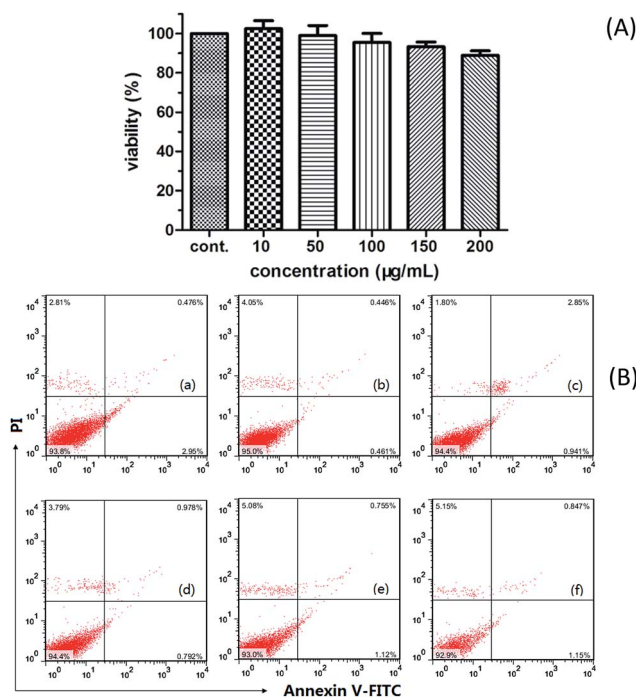

Fig. 2 Cell viability/cytotoxicity test of RAW 264.7 exposed to different concentrations of the MNP. (A) MTT shows no statistical significance was evident between the MNP treated and untreated group at concentrations from 10–200 µg mL^{-1}. (B) Analysis of the cytotoxicity induced by Fe_2O_3@DMSA on RAW 264.7 cells *via* flow cytometry after 24 h; treated and stained with Annexin V-FITC and PI. The concentrations of Fe_2O_3@DMSA from (a) to (f) were 0, 10, 50, 100, 150, 200 (µg mL^{-1}).
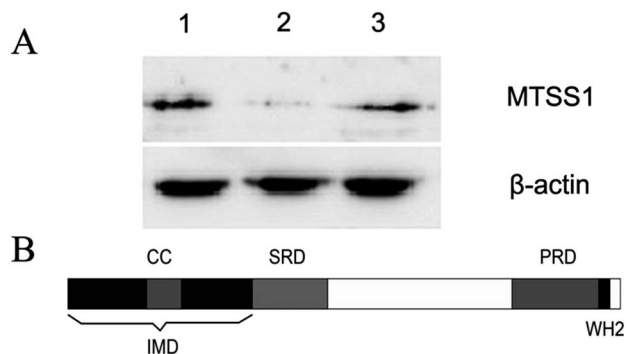
Fig. 3 The results of MIM gene expression. (A) Western blot indicated that the MIM expression was down regulated only in the RAW 264.7^{MIM-} cell line. Line 1: RAW 264.7; line 2: RAW 264.7^{MIM-}; line 3: RAW 264.7^{CKA}. (B) A drawing of the sequence domains of MIM.

Fig. 4 TEM of RAW 264.7 cells incubated with MNPs showing nanoparticles internalisation after 24 h.

mL^{-1}. Compared to the controls, there was no significant increase in apoptosis and necrosis.

The biocompatibility of nanomaterials is an important factor for *in vivo* applications. The MTT and apoptosis assays were used to evaluate the cytotoxicity of Fe$_2$O$_3$@DMSA NPs, and the results showed that the Fe$_2$O$_3$@DMSA NPs possess good biocompatibility, with almost no cytotoxicity at the test concentrations. After incubation at a high concentration of 200 μg mL^{-1} for 24 h, the viability of RAW 264.7 cells still remained above 85%.

3.3 Establishment of the MIM knock-down cell line

After shRNA transfection and puromycin selection, we obtained two stably transfected cell lines, the MIM knock down cell line RAW 264.7^{MIM-} and a control cell line RAW 264.7^{CKA}. The control shRNA plasmid-A encodes a scrambled ShRNA sequence that will not lead to a specific degradation of any known cellular mRNA. The Western blot was used to verify the effect of RNAi. The result of MIM gene expression knockdown is shown in Fig. 3.

3.4 Cellular uptake of MNPs

Transmission electron microscopy. The uptake of MNPs were confirmed by the transmission electron microscopy images taken at 24 h, as shown in Fig. 4. The images showed that the MNPs were internalised within the RAW 264.7 after 24 h. The MNPs were clearly visible and distinct from the cellular matter because of their high electron density. The high magnification image in the right panel shows the MNP aggregation and capture into vesicles inside the cells.

Prussian blue staining of intracellular Fe content. After the 24 h treatment with Fe$_2$O$_3$@DMSA, both RAW 264.7 and RAW 264.7^{MIM-} cells were stained by Prussian blue. The concentrations of Fe$_2$O$_3$@DMSA were 0, 10, 50, 100, 150, and 200 (μg mL^{-1}). The results showed that the MNPs were internalized by the cells, and as the incubation concentration increased, more MNPs were enveloped *via* endocytosis in both RAW 264.7 and RAW 264.7^{MIM-} cells. Comparing Fig. 5A and B, we find that the degree of Prussian blue staining is different, especially in the
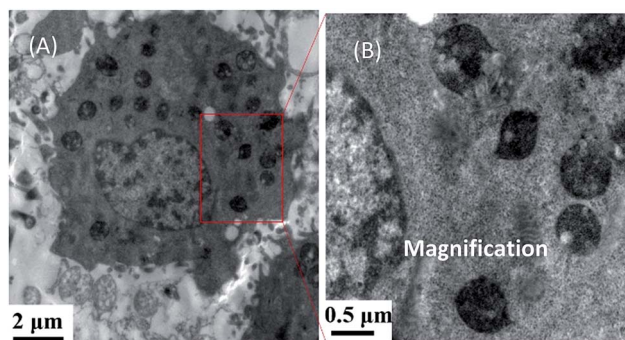
concentration of 100–200 μg mL^{-1}. The blue colour is lighter in Fig. 5B, which means that the normal RAW 264.7 cells uptake more MNPs than RAW 264.7^{MIM-} cells, indicating that the silence of the MIM expression had a negative influence on the MNPs uptake process.

Fe content determined by *o*-phenanthroline photometric method. The cellular uptake amount was measured based on the iron concentrations per milligram of protein that was internalized by the cells.[41] For the Fe$_2$O$_3$@DMSA, the cellular uptake of MNPs by all the cell lines increased with increasing concentration from 0 μg mL^{-1} to 200 μg mL^{-1} in normal medium, as shown in Fig. 6. Briefly, the cellular uptake shows
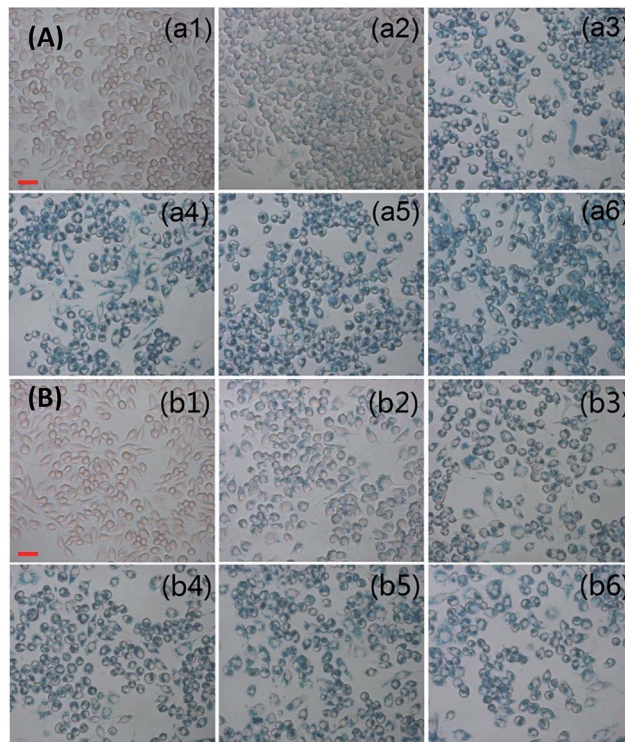

Fig. 5 Cells stained by Prussian blue after 24 h treated with MNPs. (A) was the RAW 264.7 cell line, (B) was the RAW 264.7^{MIM-} cell line. The concentrations of Fe$_2$O$_3$@DMSA (1 to 6) were 0, 10, 50, 100, 150, 200 (μg mL^{-1}). After incubation, cells stained with Prussian blue and photographed under light microscope. Scale bar = 50 μm.
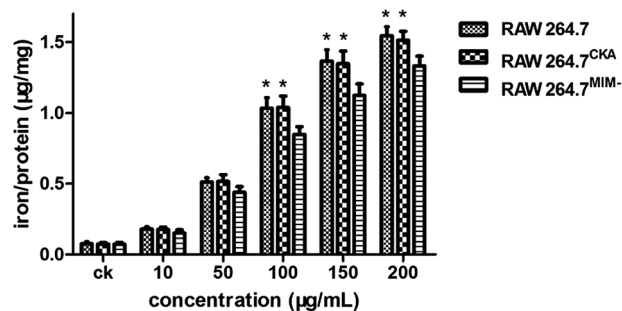
Fig. 6 The results of MNPs uptake of RAW 264.7, RAW 264.7^{CKA} and RAW 264.7^{MIM-} determined by o-phenanthroline photometric method. Data are shown as the mean ± SD, *$P < 0.05$ compared to the RAW 264.7^{MIM-} group. Control columns mean that cells were incubated with only DMEM.

Fig. 7 Flow cytometric analysis of Fe$_2$O$_3$@DMSA uptake into RAW 264.7 and RAW 264.7^{MIM-} cells analysed by side scatter after 24 h exposure. The concentration of Fe$_2$O$_3$@DMSA from (a) to (f) are 0, 10, 50, 100, 150, 200 (µg mL^{-1}).

a clear dose dependent pattern under the experiment conditions. At the incubation concentrations of 0, 10 and 50 µg mL^{-1}, there was no statistical difference among all the three groups in the MNPs uptake. At the incubation concentrations of 100, 150, and 200 µg mL^{-1}, there was a statistical significant difference ($P < 0.05$) between the RAW 264.7^{MIM-} group and the two control groups (RAW 264.7 and RAW 264.7^{CKA} group), and the iron content was lower in RAW264.7^{MIM-} than in the two control groups. In the control groups, there was no statistical difference between the RAW 264.7 group and RAW 264.7^{CKA} group at all test incubation concentrations.

Cellular uptake of MNPs analysis by SSC measurement. MNPs were enveloped by endocytosis by RAW 264.7 and RAW 264.7^{MIM-} cells as shown by the increase in average side scattering compared with the control groups with only the medium. The peak value shifts right as the Fe$_2$O$_3$@DMSA concentration increased. This result indicates that when cells were exposed to MNPs, the MNPs can be internalized by both RAW 264.7 and RAW 264.7^{MIM-} cells, shown as an increase in the SSC or the peak value right shift in Fig. 7.

When compared to the normal RAW 264.7 cells, the SSC value of RAW 264.7^{MIM-} cells is lower at all the test Fe$_2$O$_3$@-DMSA concentrations. The peak of the RAW 264.7^{MIM-} cells has less horizontal displacement than the RAW 264.7 cells. The change in the horizontal displacement was mild in RAW 264.7^{MIM-} cells compared to RAW 264.7 cells, especially in high concentrations (100–200 µg mL^{-1}). This phenomenon indicates that the uptake ability between RAW 264.7 and RAW 264.7^{MIM-} cells became significantly different in the situation of high MNPs concentration, which is consistent with the results of the o-phenanthroline photometric method described earlier.

Mechanism of uptake. Under flow cytometry, the macrophages pretreated with phenylarsine oxide (PAO) exhibited a decreased SSC compared to the control. In contrast, no significant changes in SSC were found in the cytochalasine D (cyt D), nocodazole (noco), or genistein treated macrophages (Fig. 8). This finding suggested that the clathrin receptor plays a major role in the mechanism of cellular uptake of MNPs particles.
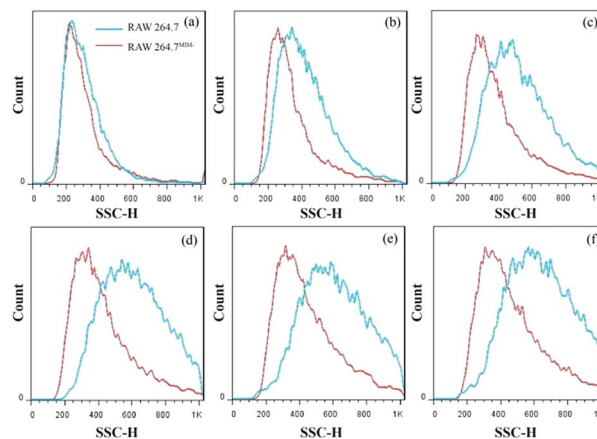
Immunofluorescence and co-localization assays. To determine the effect of MIM in cellular uptake of MNPs and find the relationship between MIM and the clathrin-mediated endocytosis pathway, MIM and clathrin were stained with anti-MTSS1/FITC antibody and anti-clathrin/RBITC, respectively (shown in Fig. 9). After they were incubated with the MNPs, MIM were recruited to the cell membrane, co-localization with clathrin (Fig. 9c), which indicated that MIM may be involved in clathrin-mediated endocytosis.
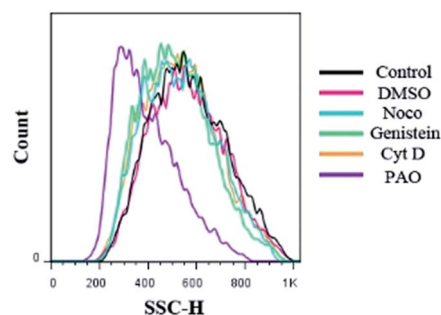

Fig. 8 The endocytotic pathway of MNP uptake in RAW 264.7 was measured by SSCs via flow cytometry after the cells were treated with different endocytotic inhibitors.
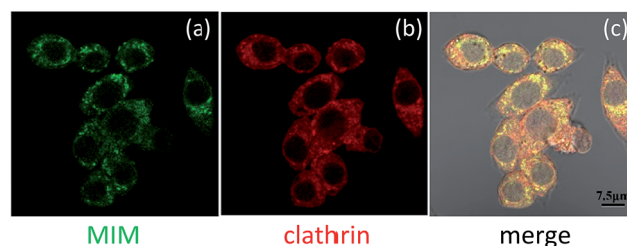

Fig. 9 Co-localization of MIM and clathrin. Cells incubated with MNPs and stained for MIM (green) and clathrin (red).

4. Discussion

Endocytosis is an important cellular process, especially in phagocytes. MIM is thought to be involved in this process. With studies of structural bioinformatics, researchers have discovered that MIM is a multifunctional protein and is an integral part in actin monomer recruitment and polymerisation by interactions among the different domains, such as WH2, PRD, SRD, and IMD (as shown in Fig. 3B). The WH2 domain is a highly evolutionarily conserved actin monomer-binding motif, which can be regulated by the Rho-family GTPase, involving the common signal pathway for actin polymerization.[42] The PRD domain of MIM can bind and activate cortactin, which can activate the actin nucleation ability of Arp2/3 complex *via* direct binding[43–45] to enhance the actin polymerization.[46] IMD also plays a key role in actin reorganization, which can induce the formation of tightly packed F-actin bundles *via* binding and activating the small GTPase Rac and form the core structure of cellular protrusions such as filopodia, microvilli, and microspikes.[47–49] Actin polymerization is associated with cytoskeletal organization and affects endocytosis processes, including phagocytosis and pinocytosis.[17,18]

As mentioned above, a large number of studies have indicated that MIM is associated with cellular endocytosis. However, there is still an argument if MIM plays a positive role in the endocytosis process. We depleted endogenous MIM in RAW 264.7 cells *via* lentiviral shRNA infection to further examine the exact effects of MIM in the MNPs uptake process. The results of prussian blue staining of intracellular iron contents and SSC measurement indicated that the normal RAW 264.7 cells uptake more MNPs than RAW 264.7[MIM-] cells, especially in the concentrations of 100–200 μg mL^{-1}. The results of the calcein fluorescence quenching assay (Fig. S2†) show the degree of fluorescence quenching was faster in normal RAW 264.7 cells than that of RAW 264.7[MIM-] cells, indicating that normal RAW 264.7 cells use endocytosis on more MNPs than RAW 264.7[MIM-] cells at the same time. All the results above revealed that the silence of MIM expression in RAW 264.7 cells had a negative influence on the MNPs uptake process. Endocytic internalization is accompanied by a transient burst of actin polymerization,[50] and the Arp2/3 complex accelerated the nucleation of actin filaments. IMD has a high affinity for PI(4,5)P2, and the oligomerization of IMD can induce large scale of PI(4,5)P2 clusters in the membrane, which can bend the membrane and induce protrusions with its positively charged convex geometry,[48,51,52] even in absence of actin.[22] The increase in the PI(4,5)P2 density is considered to promote the Arp2/3 complex-mediated actin polymerization, which is necessary for MIM-potentiated membrane protrusion elongation.[53] In the structure, the actin and PI(4,5)P2-binding sites overlap on the surface of the IMD, and the initial IMD-mediated membrane deformation may be followed by actin polymerization into the space generated.[20] In short, MIM actively generates membrane curvature through IMD domains and efficiently induces the formation of protrusions in cell membranes together with the actin polymerization. MIM provided possible links between the membrane deformation, and the actin cytoskeleton is implicated in cellular endocytosis.[51,54,55]

The iron contents of the RAW 264.7[MIM-] groups are significantly lower ($P < 0.05$) than both control groups (shown in Fig. 6) when the concentrations of MNPs range from 100–200 μg mL^{-1}. There was no statistical difference between the RAW 264.7 group and RAW 264.7[CKA] group at all tested incubation concentrations. These results showed that the silence of MIM expression in RAW 264.7 cells can inhibit the nanoparticles' endocytosis process, both in the uptake rate and uptake efficiency. Nanoparticles utilized multiple mechanisms for cellular entry,[16] such as phagocytosis, pinocytosis, and caveolae-dependent or clathrin-mediated endocytosis. The exact pathway MIM affected in endocytosis is still unclear. In Fig. 8, there was a left shift in the cell distribution following treatment with the clathrin inhibitor phenylarsine oxide prior to MNPs incubation. The other inhibitors tested showed no effect on cellular granularity. This may indicate that MNPs were internalized into macrophage RAW 264.7 *via* the clathrin-mediated pathway. Yang[56] also found out that the clathrin-mediated pathway was the main pathway for ferucarbotran to enter the macrophage.

BAR domain (include the IMD domain) proteins can be recruited to the site of endocytosis, which occurs after clathrin assembly,[57,58] and then may induce the membrane curvature and activate the actin polymerization, resulting in vesicle formation and fission releases or fusion with the endolysosome.[54,59,60] Fig. 9 clearly shows the co-localization of MIM and clathrin. The IMD/MIM take part in the clathrin-mediated endocytosis, which was the main pathway to uptake MNPs in macrophages.[14,61] In our research, when the MIM expression was silenced in RAW 264.7 cells, the MNPs uptake process was inhibited. Combined with the previous reports, we supposed that MIM inhibited the nanoparticles uptake process in macrophages mainly *via* the clathrin-mediated pathway.

5. Conclusions

In conclusion, the knock-down of MIM expression in RAW 264.7 could affect the endocytosis process for iron oxide nanoparticles in both uptake rate and uptake efficiency. MIM played a positive role in the nanoparticle uptake process. We supposed that the silence of MIM inhibited the MNPs uptake process mainly *via* the clathrin-mediated pathway, and this was important for nanoparticle applications *in vivo*, such as accumulation in target sites, prolong the circulating time, *etc.*

Acknowledgements

References

1 N. Luciani, F. Gazeau and C. Wilhelm, *J. Mater. Chem.*, 2009, **19**, 6373.

2 L. M. Pernia, S. Rivera-Fernandez, J. M. Franco, D. Pozo, J. M. de la Fuente and M. L. Garcia-Martin, *Nanoscale*, 2015, **7**, 2050–2059.

3 M. Ma, Y. Zhang, X. Shen, J. Xie, Y. Li and N. Gu, *Nano Res.*, 2015, **8**, 600–610.

4 L. Li, W. Jiang, K. Luo, H. Song, F. Lan, Y. Wu and Z. Gu, *Theranostics*, 2013, **3**, 595–615.

5 S. Jo, S. Noh, Z. Jin, Y. Lim, J. Cheon and H. Kim, *Sens. Actuators, B*, 2014, **201**, 144–152.

6 F. Yang, M. Li, H. Cui, T. Wang, Z. Chen, L. Song, Z. Gu, Y. Zhang and N. Gu, *Sci. China Mater.*, 2015, **58**, 467–480.

7 D. Liu, W. Wu, X. Chen, S. Wen, X. Zhang, Q. Ding, G. Teng and N. Gu, *Nanoscale*, 2012, **4**, 2306.

8 V. I. Shubayev, T. R. Pisanic and S. Jin, *Adv. Drug Delivery Rev.*, 2009, **61**, 467–477.

9 B. Wang, X. He, Z. Zhang, Y. Zhao and W. Feng, *Acc. Chem. Res.*, 2013, **46**, 761–769.

10 C. D. Walkey, J. B. Olsen, H. Guo, A. Emili and W. C. Chan, *J. Am. Chem. Soc.*, 2012, **134**, 2139–2147.

11 L. Lartigue, C. Wilhelm, J. Servais, C. Factor, A. Dencausse, J. Bacri, N. Luciani and F. Gazeau, *ACS Nano*, 2012, **6**, 2665–2678.

12 M. Bartneck, H. A. Keul, G. Zwadlo-Klarwasser and J. Groll, *Nano Lett.*, 2010, **10**, 59–63.

13 S. D. Conner and S. L. Schmid, *Nature*, 2003, **422**, 37–44.

14 F. Zhao, Y. Zhao, Y. Liu, X. Chang, C. Chen and Y. Zhao, *Small*, 2011, **7**, 1322–1337.

15 S. Mayor and R. E. Pagano, *Nat. Rev. Mol. Cell Biol.*, 2007, **8**, 603–612.

16 G. Sahay, D. Y. Alakhova and A. V. Kabanov, *J. Controlled Release*, 2010, **145**, 182–195.

17 V. Jaumouillé and S. Grinstein, *Curr. Opin. Cell Biol.*, 2011, **23**, 22–29.

18 S. Mayor, R. G. Parton and J. G. Donaldson, *Cold Spring Harbor Perspect. Biol.*, 2014, **6**, a016758.

19 A. Frost, R. Perera, A. Roux, K. Spasov, O. Destaing, E. H. Egelman, P. De Camilli and V. M. Unger, *Cell*, 2008, **132**, 807–817.

20 Y. Rao and V. Haucke, *Cell. Mol. Life Sci.*, 2011, **68**, 3983–3993.

21 P. D. Blood and G. A. Voth, *Proc. Natl. Acad. Sci. U. S. A.*, 2006, **103**, 15068–15072.

22 J. Saarikangas, H. Zhao, A. Pykäläinen, P. Laurinmäki, P. K. Mattila, P. K. J. Kinnunen, S. J. Butcher and P. Lappalainen, *Curr. Biol.*, 2009, **19**, 95–107.

23 J. Linkner, G. Witte, H. Zhao, A. Junemann, B. Nordholz, P. Runge-Wollmann, P. Lappalainen and J. Faix, *J. Cell Sci.*, 2014, **127**, 1279–1292.

24 K. D. Mertz, G. Pathria, C. Wagner, J. Saarikangas, A. Sboner, J. Romanov, M. Gschaider, F. Lenz, F. Neumann, W. Schreiner, M. Nemethova, A. Glassmann, P. Lappalainen, G. Stingl, J. V. Small, D. Fink, L. Chin and S. N. Wagner, *Nat. Commun.*, 2014, **5**, 3465.

25 L. M. Machesky and S. A. Johnston, *J. Mol. Med.*, 2007, **85**, 569–576.

26 M. Cao, T. Zhan, M. Ji and X. Zhan, *Biochem. J.*, 2012, **446**, 469–475.

27 L. M. Machesky and S. A. Johnston, *J. Mol. Med.*, 2007, **85**, 569–576.

28 J. C. Dawson, P. Timpson, G. Kalna and L. M. Machesky, *Oncogene*, 2012, **31**, 1781–1793.

29 J. Zhong, S. Shaik, L. Wan, A. E. Tron, Z. Wang, L. Sun, H. Inuzuka and W. Wei, *OncoTargets Ther.*, 2013, **4**, 2339–2353.

30 D. Yu, X. H. Zhan, X. F. Zhao, M. S. Williams, G. B. Carey, E. Smith, D. Scott, J. Zhu, Y. Guo, S. Cherukuri, C. I. Civin and X. Zhan, *Oncogene*, 2011, **31**, 3561–3568.

31 Y. Li, Z. Chen and N. Gu, *Chin. Sci. Bull.*, 2012, **57**, 3972–3978.

32 J. W. Liu, Y. Zhang, D. Chen, T. Yang, Z. P. Chen, S. Y. Pan and N. Gu, *Colloids Surf., A*, 2009, **341**, 33–39.

33 O. Zurkiya, A. W. S. Chan and X. Hu, *Magn. Reson. Med.*, 2008, **59**, 1225–1231.

34 T. K. Jain, M. K. Reddy, M. A. Morales, D. L. Leslie-Pelecky and V. Labhasetwar, *Mol. Pharmaceutics*, 2008, **5**, 316–327.

35 N. Nitin, L. E. W. LaConte, O. Zurkiya, X. Hu and G. Bao, *JBIC, J. Biol. Inorg. Chem.*, 2004, **9**, 706–712.

36 A. Beduneau, Z. Ma, C. B. Grotepas, A. Kabanov, B. E. Rabinow, N. Gong, R. L. Mosley, H. Dou, M. D. Boska and H. E. Gendelman, *PLoS One*, 2009, **4**, e4343.

37 M. Wang, M. Cao, Z. Guo and N. Gu, *Chin. Sci. Bull.*, 2013, **58**, 2663–2666.

38 Y. Yan, K. T. Gause, M. M. J. Kamphuis, C. Ang, N. M. O'Brien-Simpson, J. C. Lenzo, E. C. Reynolds, E. C. Nice and F. Caruso, *ACS Nano*, 2013, **7**, 10960–10970.

39 M. S. Lord, M. Jung, W. Y. Teoh, C. Gunawan, J. A. Vassie, R. Amal and J. M. Whitelock, *Biomaterials*, 2012, **33**, 7915–7924.

40 J. Rejman, V. Oberle, I. S. Zuhorn and D. Hoekstra, *Biochem. J.*, 2004, **377**, 159–169.

41 S. Zhang, X. Chen, C. Gu, Y. Zhang, J. Xu, Z. Bian, D. Yang and N. Gu, *Nanoscale Res. Lett.*, 2009, **4**, 70–77.

42 E. Paunola, P. K. Mattila and P. Lappalainen, *FEBS Lett.*, 2002, **513**, 92–97.

43 R. L. Jeng and M. D. Welch, *Curr. Biol.*, 2001, **11**, R691–R694.

44 T. Uruno, J. Liu, P. Zhang, Y. Fan, C. Egile, R. Li, S. C. Mueller and X. Zhan, *Nat. Cell Biol.*, 2001, **3**, 259–266.

45 E. Derivery, C. Sousa, J. J. Gautier, B. Lombard, D. Loew and A. Gautreau, *Dev. Cell*, 2009, **17**, 712–723.

46 J. Lin, J. Liu, Y. Wang, J. Zhu, K. Zhou, N. Smith and X. Zhan, *Oncogene*, 2005, **24**, 2059–2066.

47 A. Yamagishi, M. Masuda, T. Ohki, H. Onishi and N. Mochizuki, *J. Biol. Chem.*, 2004, **279**, 14929–14936.

48 P. K. Mattila, A. Pykalainen, J. Saarikangas, V. O. Paavilainen, H. Vihinen, E. Jokitalo and P. Lappalainen, *J. Cell Biol.*, 2007, **176**, 953–964.

49 G. Bompard, *J. Cell Sci.*, 2005, **118**, 5393–5403.

50 J. Toshima, J. Y. Toshima, A. C. Martin and D. G. Drubin, *Nat. Cell Biol.*, 2005, **7**, 246–254.

51 F. Safari and S. Suetsugu, *Membranes*, 2012, **2**, 91–117.

52 J. Saarikangas, H. Zhao, A. Pykalainen, P. Laurinmaki, P. K. Mattila, P. K. Kinnunen, S. J. Butcher and P. Lappalainen, *Curr. Biol.*, 2009, **19**, 95–107.

53 J. Saarikangas, N. Kourdougli, Y. Senju, G. Chazal, M. Segerstråle, R. Minkeviciene, J. Kuurne, P. K. Mattila, L. Garrett, S. M. Hölter, L. Becker, I. Racz, W. Hans, T. Klopstock, W. Wurst, A. Zimmer, H. Fuchs, V. Gailus-Durner, M. Hrabĕ De Angelis, L. von Ossowski, T. Taira, P. Lappalainen, C. Rivera and P. Hotulainen, *Dev. Cell*, 2015, **33**, 644–659.

54 H. Zhao, A. Pykäläinen and P. Lappalainen, *Curr. Opin. Cell Biol.*, 2011, **23**, 14–21.

55 S. H. Lee, F. Kerff, D. Chereau, F. Ferron, A. Klug and R. Dominguez, *Structure*, 2007, **15**, 145–155.

56 C. Y. Yang, M. F. Tai, C. P. Lin, C. W. Lu, J. L. Wang, J. K. Hsiao and H. M. Liu, *PLoS One*, 2011, **6**, e25524.

57 S. M. Ferguson, A. Raimondi, S. Paradise, H. Shen, K. Mesaki, A. Ferguson, O. Destaing, G. Ko, J. Takasaki, O. Cremona, T. E. O' and P. De Camilli, *Dev. Cell*, 2009, **17**, 811–822.

58 M. V. Douwe, A. Giulio, J. S. Heather, M. M. Laura, Z. R. Joshua and H. I. Robert, *Biochem. J.*, 2011, **436**, 45–52.

59 S. Suetsugu, K. Toyooka and Y. Senju, *Semin. Cell Dev. Biol.*, 2010, **21**, 340–349.

60 J. C. Dawson, J. A. Legg and L. M. Machesky, *Trends Cell Biol.*, 2006, **16**, 493–498.

61 S. A. Mousavi, L. Malerod, T. Berg and R. Kjeken, *Biochem. J.*, 2004, **377**, 1–16.